RSC Advances

PAPER

View Article Online
View Journal | View Issue

Cite this: *RSC Adv.*, 2017, **7**, 48324

Synthesis of sustainable lignin-derived mesoporous carbon for supercapacitors using a nano-sized MgO template coupled with Pluronic F127†

Yaoguang Song, Junli Liu,* Kang Sun and Wei Xu

Received 26th August 2017
Accepted 9th October 2017

DOI: 10.1039/c7ra09464g

rsc.li/rsc-advances

Herein, we describe the synthesis of meso-structured carbon from residual pre-cross-linked lignin from a wheat straw alkaline pulping process by employing nano-sized MgO and Pluronic F127 as templates. MgO nano-particles function as substrates and the main template by a space occupying effect, while F127 works as a dispersant preventing the agglomeration of MgO as well as a soft templating agent. To the best of our knowledge, no work concerning the synthesis of lignin-derived mesoporous carbon *via* a MgO template route has been reported. The mass ratio of lignin/MgO plays a major role in enriching the porosity of the carbon. Vacuum drying and freeze-drying technologies were applied during solvent evaporation to ensure the Mg template can be dispersed sufficiently. The Brunauer–Emmett–Teller specific surface area and total pore volume can reach 712 $m^2\ g^{-1}$ and 0.90 $cm^3\ g^{-1}$, with a mesopore content of over 83%. The electrochemical performance of the obtained carbons as supercapacitor electrode materials was investigated. Although the vacuum environment enhanced the porosity and pore uniformity, the corresponding carbon didn't exhibit better electrochemical behavior than the carbon derived without a vacuum environment.

1. Introduction

The irreversible depletion of fossil fuels and ever-increasing concentration of key greenhouse gases in the atmosphere have impelled the conversion of lignocellulosic biomass feedstock and the reutilization of waste biomass resources for energy applications to meet human's daily energy consumption demands.[1,2] Besides cellulose and hemicellulose, lignin is one of the three recalcitrant components of lignocellulosic biomass and the most abundant heterogeneous aromatic structural biopolymer in the natural world. In addition, lignin, as an almost unlimited residual byproduct of the pulp and paper industry, with a total global yield of about 50 billion tons per year, and in particular over 5 million tons in China,[3] constitutes 30% of non-fossil organic carbon and is inefficient as a solid fuel to supply energy by burning.[4,5] Deriving more value from lignin therefore has successfully caught worldwide attention.[6–10]

Lignin has a high carbon content over 50% (ref. 11) and becomes one of the most promising ideal precursors for carbonaceous materials. Microporous carbon materials (*e.g.* conventional activated carbons) are ideally suited to liquid and gas-phase adsorption but have industrial limited applications including biomedical devices, catalysis, and electrochemical partially due to the requirement for mesopores.[2] Particularly, mesoporous carbons as electrode materials for supercapacitors show higher capacitance retention and excellent rate performance at high current density.[12–15] Preparing mesoporous carbons from sustainable lignin therefore has interested researchers worldwide, especially through nano-casting techniques, which commonly employ sacrificial silica[16–19] or amphiphilic surfactants[20–22] to tailor the pore texture precisely.

Unlike linear polysaccharides, lignin is a complicated amorphous polymer, composed of phenylpropanolic units linked by ether and C–C bonds.[6] Regardless of some negative aspects of hard template route such as multiple synthesis steps and the use of hazardous HF or NaOH,[23] it is still challenging to ensure highly branched lignin to be impregnated into narrow pores of mesoporous silica. While the soft template route based on micelle formation possesses inherent limitations on choosing ideal template surfactants and carbon precursors,[23,24] which are mostly phenolic monomers (*e.g.* phenol, resorcinol and phloroglucinol) or linear polysaccharides with lower molecular weight and specific molecular structure (*e.g.* glucose and furfural). Heterogeneous molecular architecture and highly branched structure can cause imperfect self-assembly of surfactant micelles in the randomly cross-linked matrix and result in disordered pore structure and small pore volume.[22] Saha *et al.*[20,22] recently employed a commercially available amphiphilic surfactant Pluronic F127 as template to fabricate

Institute of Chemical Industry of Forest Products, CAF, National Engineering Lab. for Biomass Chemical Utilization, Key and Open Lab. on Forest Chemical Engineering, SFA, Key Lab. of Biomass Energy and Material, Jiangsu Province, Nanjing 210042, China. E-mail: liujunli@msn.com; Tel: +86-25-854828410

† Electronic supplementary information (ESI) available. See DOI: 10.1039/c7ra09464g

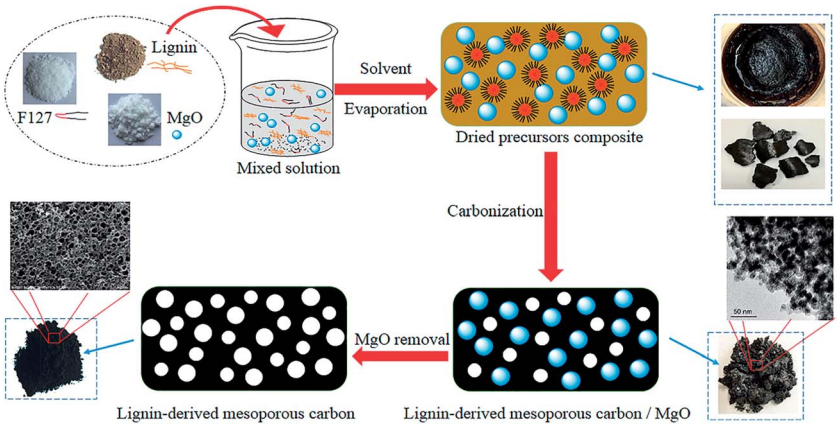

Fig. 1 Schematic of lignin-derived mesoporous carbon *via* a dual-template strategy.

mesoporous carbon from lignin in combination with formaldehyde (HCHO) as cross-linking agent. They compared it with carbons derived from a typical phenolic precursor (*i.e.* phloroglucinol) and natural hardwood pre-cross-linked lignin. The carbon with phloroglucinol precursor exhibited a narrower pore widths and a larger Brunauer–Emmett–Teller specific surface area (BET SSA) than those of lignin-derived mesoporous carbons. While, the carbon with pre-cross-linked lignin precursor showed a much smaller BET SSA than that of carbon with lower-molecular-weight fraction of lignin in combination with HCHO. The polymerization degree of lignin has a strong effect on the porosity and structure of carbon. Therefore, synthesizing lignin-derived carbons *via* porous silica template route or surfactant template route is lack of the versatility due to the highly branched structure and the diversity of lignin from different sources.

Some reports synthesized mesoporous carbons *via* hard template route employing oxides nanoparticles or salts as template, such as MgO,[25–30] Fe_2O_3,[15,31,32] and $CaCO_3$,[33,34] which is more convenient than surfactant template route or traditional porous silicon-containing templates. Particularly, the MgO template route is unconstrained by the polymerization degree of precursor, and throughout the whole carbonization, the MgO cannot react with the carbonaceous materials formed from the pyrolysis of carbon precursors and functions just as substrate.[26,28] What's more, MgO template can be easily dissolved out by diluted acid after carbonization to isolate carbon products, and availably recovered and recycled for the production of porous carbons.[26] To the best of our knowledge, no report about synthesizing lignin-derived mesoporous carbons by employing MgO as template has been found.

Herein, we describe the synthesis of mesoporous carbon from a kind of cheap and plentiful waste biomass, residual pre-cross-linked alkali lignin in wheat straw alkaline pulping process by using MgO as template additionally coupled with Pluronic F127 template ($EO_{106}PO_{70}EO_{106}$, with an average molecular weight of 12 600). The space occupying effect of MgO template is critical to enlarge the porosity of carbons. Both the soft template Pluronic F127 and MgO precursor eventually show a negligible carbon yield after carbonization.[24,26] Possible ideal synthesis mechanism schematic of this dual templates route is depicted roughly in Fig. 1. In this prevent work, $Mg(CH_3COO)_2 \cdot 4H_2O$ was selected as the precursor of MgO particles, obtained by the pyrolysis of Mg acetate below 350 °C. The functions of nano MgO and Pluronic F127, precursors mixing mass ratios, pore textural properties and electrochemical performance of as-made carbons as electrode materials on supercapacitor were discussed in detail. Our objective was to provide a new thought to synthesize lignin-derived carbon materials and to enhance the sustainability by reutilizing waste biomass.

2. Material and methods

2.1 Pretreatment of pre-cross-linked alkali lignin

80 g of initial alkali lignin powder (pH = 10.1, 3 wt% in water, Xinyi Feihuang Chemical Co., Ltd, China) was dissolved in 800 mL of deionized water and then filtered when pH was adjusted to ~7.0 with hydrochloric acid (HCl, Nanjing Chemical Reagent Co., Ltd, China). The filtrate was subsequently stirred adequately in dilute slurry form after pH was adjusted to ~2.0. Then lignin purified roughly was eventually obtained after being filtered, washed and dried at 105 °C.

Detailed properties of the lignin purified are listed in Table 1. Note that the purity including acid-soluble and acid-insoluble lignin was measured according to American National Renewable Energy Laboratory's (NREL) Laboratory Analytical Procedures.

2.2 Synthesis of lignin-derived mesoporous carbons

For a typical run, the alkali lignin powder pretreated above and Pluronic F127 were dissolved in 200 mL of THF with additional 1.34 mL of 6 M HCl. $Mg(CH_3COO)_2 \cdot 4H_2O$ was simultaneously dissolved in 300 mL of H_2O, and slowly poured into the former solution. Afterward, the mixed solution was stirred at room temperature for 24 h, and placed at 45 °C for 1 day and maintained at 70 °C until the monolithic mass was exsiccated thoroughly. Then the dried mixture mass was collected in a quartz boat and carbonized in a tube furnace under flowing nitrogen

Table 1 Purity, proximate and elemental analyses of lignin purified

		Proximate analysis (wt%)			Elemental analysis (daf, wt%)				
Carbon precursor	Purity (%)	M_{ad}	A_d	V_{daf}	C	H	S	N	O[a]
Alkali lignin	98.86	2.49	0.14	66.78	64.05	5.60	3.62	0.90	25.83

[a] By difference.

(100 mL min^{-1}). The heating profile was ramped from ambient temperature to 70 °C at 10 °C min^{-1}, 70 °C to 400 °C at 1 °C min^{-1}, 400 °C to 1000 °C at 2 °C min^{-1}, and maintained at 1000 °C for 15 min, followed by cooling down to ambient temperature. Finally, the sample was washed by using 1 M HCl solution and H_2O to dissolve the substrate MgO out, and dried at 105 °C for 24 h. The obtained carbons are labelled as LMC_{x-y-z}, where the subscript x, y and z represent the mass of lignin, MgO and Pluronic F127, respectively.

For comparison, two samples were also synthesized *via* the surfactant template route and the independent MgO template route, respectively. More concretely, the sample only using Pluronic F127 as template was fabricated by remaining all aforementioned experimental conditions identical except no Mg acetate aqueous solution added and labelled as LMC_{F127}. While, the sample *via* the independent MgO template route was made by the same experimental conditions except no Pluronic F127 added and labelled as LMC_{MgO}. Furthermore, a sample without any templating agent was also prepared by carbonizing alkali lignin powder only and labelled as LC.

2.3 Characterizations

The pore texture properties of all as-made carbons were investigated with an ASAP 2020 analyzer by N_2 adsorption–desorption isotherms at 77 K. BET SSA and differential pore size distribution were calculated respectively by using the BET equation and the density functional theory (DFT). Morphology of carbons was performed by field emission scanning electron microscopy (FESEM, Hitachi S-4800) at an accelerating voltage of 3.0 kV and by transmission electron microscopy (TEM, JEM 2100) at an accelerating voltage of 200 kV. X-ray diffraction (XRD) patterns (10–80°) and Raman spectra were obtained by a D8 Focus X-ray diffractometer equipped with Cu Kα radiation (λ = 0.154 nm) and a Thermor DXR532 Raman spectrometer with a 532 nm excitation source, respectively. X-ray photoelectron spectroscopic (XPS) data was performed by a Kratos AXIS UltraDLD K-Alpha X-ray photoelectron spectrometer in the ultrahigh vacuum of 7×10^{-8} Pa equipped with hemisphere analyzer.

2.4 Electrochemical test

The performance for supercapacitor of the obtained carbons was tested on a CHI 660D electrochemical analyzer at ambient temperature. The electrode was prepared by mixing 80 wt% carbon samples, 10 wt% acetylene black and 10 wt% PTFE, where the former two worked as an electrical conductor and the latter as a binder. In the three-electrode configuration, the counter electrode, reference electrode and electrolyte are a platinum wire, Ag/AgCl electrode, and 1 M H_2SO_4, respectively. The gravimetric capacitances (C_g, F g^{-1}) was calculated by the formula of $C_g = (I \times \Delta t)/(m \times V)$, where I (A) is discharge current, Δt (s) is the discharge time, V (V) is the potential window during discharge and m (g) is the mass of active material on electrode.

3. Results and discussion

3.1 Characterization of carbons

We successfully synthesized mesoporous carbons from pre-cross-linked lignin particles by simultaneously employing MgO nanoparticles and Pluronic F127 as structure-directing agents. Detailed pore texture properties of as-made LMCs are listed in Table 2. Obviously, samples *via* single templating method (LMC_{F127} and LMC_{MgO}) have higher porosities than LC, the sample without any templating agent. Moreover, the BET SSA and total pore volume of $LMC_{10-1-16}$, the sample synthesized with 1 g of MgO and 16 g of F127, reached 356 m^2 g^{-1} and 0.44 cm^3 g^{-1}, which are both much larger than those of LMC_{F127} and LMC_{MgO}. For comparison with LMC_{F127}, sample $LMC_{F127-HCHO}$ was simultaneously synthesized in the same way from lignin additionally in combination with HCHO as cross-linking agent, the BET SSA and total pore volume of which decreased to only 26 m^2 g^{-1} and 0.029 cm^3 g^{-1}. Similarly, $LMC_{10-1-16-HCHO}$ with HCHO added was also prepared in the same way as $LMC_{10-1-16}$ and exhibited a BET SSA of 234 m^2 g^{-1} and total pore volume of 0.23 cm^3 g^{-1}. That the decreased porosities after adding HCHO can be attributed to the highly branched lignin structure utilized in this present work and the continuous over-cross-linked lignin matrix after the cross-linking reaction. However, as shown in Fig. S1,† the solvent evaporation process during synthesizing LMC_{MgO} induced Mg acetate partially to recrystallize and agglomerate together, even in an extremely small lignin/$Mg(CH_3COO)_2 \cdot 4H_2O$ mixing ratio, directly resulting in the poor porosity of LMC_{MgO}, whose BET SSA and pore volume are still larger than LMC_{F127} though. Fig. S2† shows the TEM micrograph of sample $LMC_{10-1-16}$ before template extraction. Some distorted aperiodic pores formed from the F127 and the carbonization of lignin itself can be clearly seen. Besides, nano-sized MgO particles with size of about 11 nm are distributed disorderly and randomly. Therefore, we infer that the Pluronic F127 is critical to disperse Mg acetate sufficiently as well as functioning as the soft template, and that the amount of MgO nanoparticles may play a major role to enrich the porosity of carbons.

Table 2 Pore textural properties of LMCs

Sample	Lignin (g)	MgO (g)	F127 (g)	BET SSA (m^2 g^{-1})	V_{meso} (cm^3 g^{-1})	V_{total} (cm^3 g^{-1})	Mesopores (%)
LC	10	0	0	19	0.009	0.023	39.13
LMC_{F127}	10	0	16	59	0.070	0.087	80.46
$LMC_{F127-HCHO}$	10	0	16	26	0.013	0.029	44.83
LMC_{MgO}	10	1	0	85	0.071	0.103	68.93
$LMC_{10-1-16}$	10	1	16	356	0.35	0.44	79.55
$LMC_{10-1-16-HCHO}$	10	1	16	234	0.14	0.23	60.87
$LMC_{10-2-16}$	10	2	16	419	0.54	0.67	80.60
$LMC_{10-4-16}$	10	4	16	563	0.65	0.77	84.42
$LMC_{10-6-16}$	10	6	16	610	0.67	0.81	82.72
LMC_{10-8-8}	10	8	8	555	0.56	0.67	83.58
$LMC_{10-8-16}$	10	8	16	642	0.72	0.86	84.88
$LMC_{10-8-16, V}$	10	8	16	712	0.75	0.90	83.33
$LMC_{10-8-16, F}$	10	8	16	672	0.56	0.72	77.78
$LMC_{10-8-24}$	10	8	24	642	0.77	0.91	84.62
$LMC_{10-8-32}$	10	8	32	643	0.77	0.91	84.62
$LMC_{10-12-16}$	10	12	16	628	0.55	0.68	80.88
$LMC_{10-16-16}$	10	16	16	572	0.46	0.61	75.41
$LMC_{10-20-16}$	10	20	16	487	0.45	0.56	80.36

The derivative plots from thermogravimetric analysis (DTG) in Fig. S3† shows that $Mg(CH_3COO)_2 \cdot 4H_2O$ has total two weight loss states. The former one occurs below 200 °C, indicating the loss of its crystal water, and the latter one provides MgO nanoparticles from the decomposition of $Mg(CH_3COO)_2 \cdot 4H_2O$ at the temperature ranging from 300 °C to 350 °C. Compared with pure Pluronic F127, the DTG peak of F127 mixed together with lignin appears a 5 °C shift to the higher temperature of 366 °C, which could signify the hydrogen bonding between F127 and lignin.[24] After further adding Mg acetate, the DTG peak of the eventual precursor mixture appears at around 364 °C. Such a 2 °C shift to lower temperature of 364 °C can be attributed to the weak chelation between Mg^{2+} and lignin, and the dispersion of Mg acetate *via* the chelation with the O atoms of F127 in some extent.

To ascertain the relationship between MgO/lignin mixing ratio and the eventual corresponding pore texture properties, we remained the mass of F127 as an invariant constant and gradually increased the mixing ratio of MgO/lignin in the precursor mixture. As clearly shown in Fig. 2a, MgO/lignin mixing ratio is a crucial factor for the eventual porosity of LMCs. After adding MgO template, BET SSA and pore volume increased greatly and kept apparent growth trend at a lower dosage of $Mg(CH_3COO)_2 \cdot 4H_2O$, whereas they gradually decreased with the increasing MgO/lignin mixing mass ratio. The obtained $LMC_{10-8-16}$, the sample synthesized with 8 g of MgO and 16 g of F127, got the richest porosity with a BET SSA of 642 m^2 g^{-1} and a total pore volume of 0.86 cm^3 g^{-1}, including a mesopore volume of 0.72 cm^3 g^{-1}.

Pluronic F127 functions as dispersant to prevent the agglomeration of Mg acetate as well as soft template agent. Therefore, the dosage of F127 is another key factor affecting the eventual porosity of carbons. Fig. 2b depicts the relationship between F127/MgO mixing ratio and the corresponding BET SSA and pore volume of carbons. Compared with LMC_{MgO}, the sample without F127, the using of F127 template substantially dispersed Mg acetate and enlarged the porosity of carbons. But on the whole, with F127/MgO mixing ratio increasing, the BET SSA and pore volume kept relatively steady and little growth.

In order to ensure Mg acetate can be dispersed well, vacuum drying and freeze-drying technologies were applied for the comparison with atmospheric pressure environment during solvent evaporation. The movement of Mg^{2+} in solution at higher temperature is much faster than that at lower temperature. During solvent evaporation, both vacuum drying and freeze-drying can significantly reduce the temperature, control

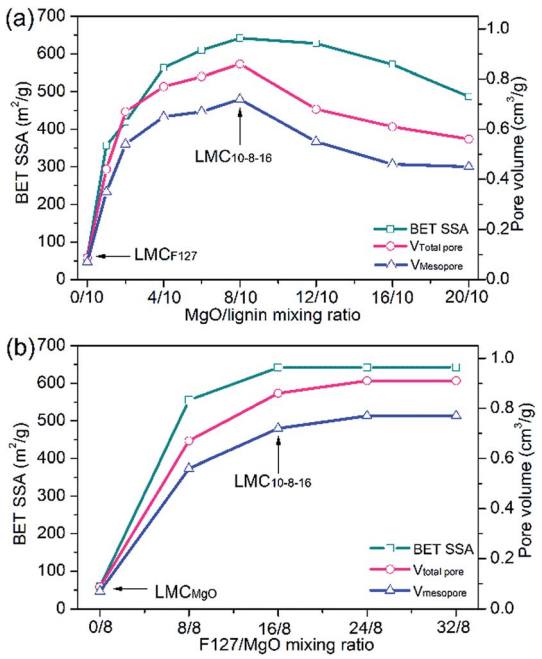

Fig. 2 (a) Optimal level of MgO/lignin mixing ratio and (b) optimal level of F127/MgO mixing ratio as determined from BET SSA, mesopore and total pore volume.

the drying rate of solvent, and therefore restrain the fast movement of Mg^{2+} to prevent its agglomeration. Especially, freeze drying can preserve the skeleton of the entire composite of precursors and keep Mg^{2+} in its own space fixed. Two groups of samples were synthesized by the same precursors mixing mass ratio and experimental condition as $LMC_{10-8-16}$, except that one of the two mixed precursors solutions was exsiccated by vacuum drying at 45 °C (labelled as $LMC_{10-8-16,\ V}$) and the other by vacuum freeze-drying (labelled as $LMC_{10-8-16,\ F}$), respectively. Results indicate that ways to exsiccate the precursor mixture liquid exert an implication to the eventual porosity of as-made carbons. $LMC_{10-8-16,\ V}$ exhibits a mesopore volume of 0.75 $cm^3\ g^{-1}$, with BET SSA of 712 $m^2\ g^{-1}$ and total pore volume of 0.90 $cm^3\ g^{-1}$, which are larger than those of $LMC_{10-8-16}$. The higher porosity of $LMC_{10-8-16,\ V}$ indicates that vacuum environment promoted the development of pores and enlarged the porosity of carbon. While freeze drying kept each component in its own space fixed, and significantly hindered the spontaneous agglomeration of template during solvent evaporation. However, the mesopore and total pore volume of obtained $LMC_{10-8-16,\ F}$ decreased to 0.56 $cm^3\ g^{-1}$ and 0.72 $cm^3\ g^{-1}$, respectively, which are both smaller than those of $LMC_{10-8-16}$. The lower porosity of freeze-dried sample indicates that vacuum freezing environment may hinder the enlargement of porosity. As mentioned before, Saha *et al.*[20] fabricated mesoporous carbon from solvent-extracted lower-molecular-weight fraction of lignin *via* surfactant template route. The corresponding optimal carbon exhibits a BET SSA of 418 $m^2\ g^{-1}$ and a mesopore volume of 0.34 $cm^3\ g^{-1}$, which are still much smaller than our best result *via* dual templates route.

Fig. 3a depicts the N_2 adsorption–desorption isotherms of N_2 at 77 K for selected LMCs. The obvious hysteresis loops, typical feature of type IV (according to IUPAC classification), confirm the presence of mesoporosity. Fig. 3b indicates the dominant well-developed mesopore structure. LMC_{F127} as well as LMC_{MgO} has a broad pore size distributions, while $LMC_{10-1-16}$ shows dominant peaks around 9 nm. Compared with $LMC_{10-8-16}$ and $LMC_{10-8-16,\ F}$, $LMC_{10-8-16,\ V}$ exhibits a narrower and smaller pore size distribution ranging from 6 nm to 11 nm due to the enhanced dispersibility under 45 °C vacuum environment during solvent evaporation.

As shown in Fig. 4a, layer-stacking surface structures with slit-like pores are visible clearly in LMC_{F127} because of the lack of MgO substrates to support carbon frameworks and partial pore structures shrinkage and collapse. LMC_{MgO} also shows some rare random pores (Fig. S4a†) as LMC_{F127} due to the partial recrystallization and agglomeration of Mg acetate. Moreover, pores in LC (Fig. S4b†), the sample without any templating agent, are rarer than both LMC_{F127} and LMC_{MgO}. However, $LMC_{10-8-16}$ synthesized *via* dual templates route has a much more developed pore structures and a better pore structure connectivity (Fig. 4b). TEM image (Fig. 4e) depicts that $LMC_{10-8-16}$ is abundant with worm-like disordered aperiodic pores. While pores in $LMC_{10-8-16,\ V}$ are relatively more regular and uniform (Fig. 4c and f), which indicates that vacuum environment during solvent evaporation can enhance the uniformity of templates and therefore induce a narrower pore size distribution. As shown in Fig. 4d and S4c,† pores in $LMC_{10-8-16,\ F}$ are much complex, and some open large pores larger than 100 nm are also noticeable. These large pores can be

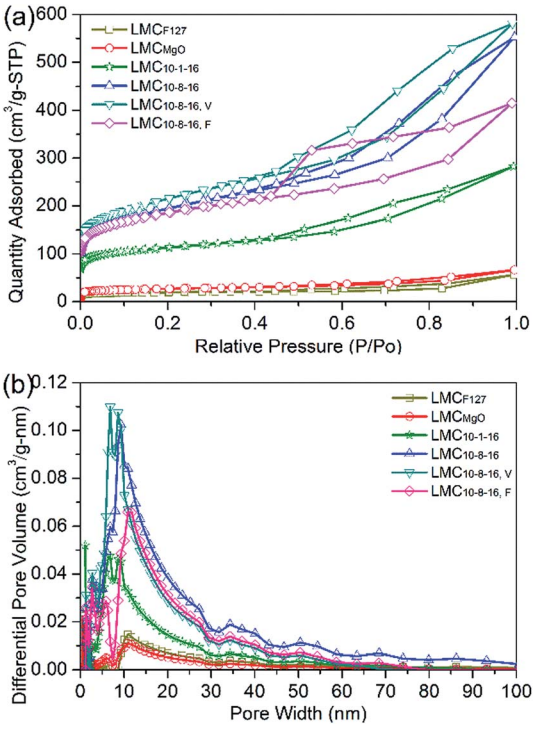

Fig. 3 (a) N_2 adsorption–desorption isotherms with (b) differential pore size distributions for the selected typical LMCs.

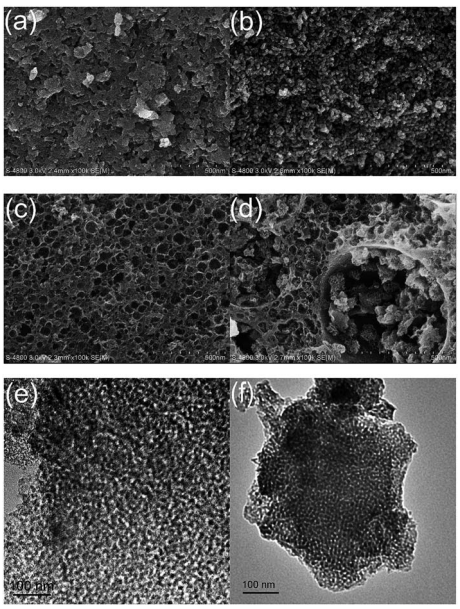

Fig. 4 FESEM micrographs for (a) LMC_{F127}, (b) $LMC_{10-8-16}$, (c) $LMC_{10-8-16,\ V}$ and (d) $LMC_{10-8-16,\ F}$; TEM micrographs for (e) $LMC_{10-8-16}$ and (f) $LMC_{10-8-16,\ V}$.

attributed to the inevitable change of liquid solvent into solid ice crystals during freezing and the further sublimation of certain ice crystals with particle size over 100 nm after drying completely.

Wide-angle XRD patterns for obtained LMCs are shown in Fig. 5a. Broad diffraction peaks can be obviously seen at $2\theta = 24^\circ$ and 44°, typical (002) and (100) diffraction of graphitic carbon.[35] The XRD patterns of LMC_{F127} and LMC_{MgO} are consistent with typical nanostructured mesoporous non-graphitized carbon black (NMCB) powders,[36] exhibiting a strong and sharp peak at $2\theta = 45^\circ$. However, there are no strong and sharp peaks in XRD patterns for other LMCs, indicating the dominating amorphous carbon structure of samples. Fig. 5b is the Raman spectra of all carbons. The G band at around 1590 cm^{-1} is derived from bond stretching of sp^2 carbon pairs in both rings and chains, implying the presence of graphitic structure, and the D band at around 1350 cm^{-1} is induced by the breathing mode of aromatic rings, indicating the lattice defects due to structure distortion.[19,37,38] Therefore, the peak intensity ratio of D band to G band usually acts as a measure for disorder degree or graphitization degree. As listed in Table S1,† the I_D/I_G values of all LMCs are very close to each other, and demonstrate that precursors mixing ratios as well as ways to exsiccate the precursor mixing liquids have little effect on the graphitization degree of obtained carbons. The overall XPS survey spectra in Fig. 5c as well as Table S2† reveals the presence of dominating carbon and significant presence of oxygen. A high surface oxygen content can improve surface wettability in aqueous solutions. However, after four times of measurements for each sample, the average oxygen contents are statistically similar and range from 16.05% to 20.29%, which indicates that under the same carbonization conditions, different preparation methods provided in this work have little effect on the oxygen contents of obtained carbons.

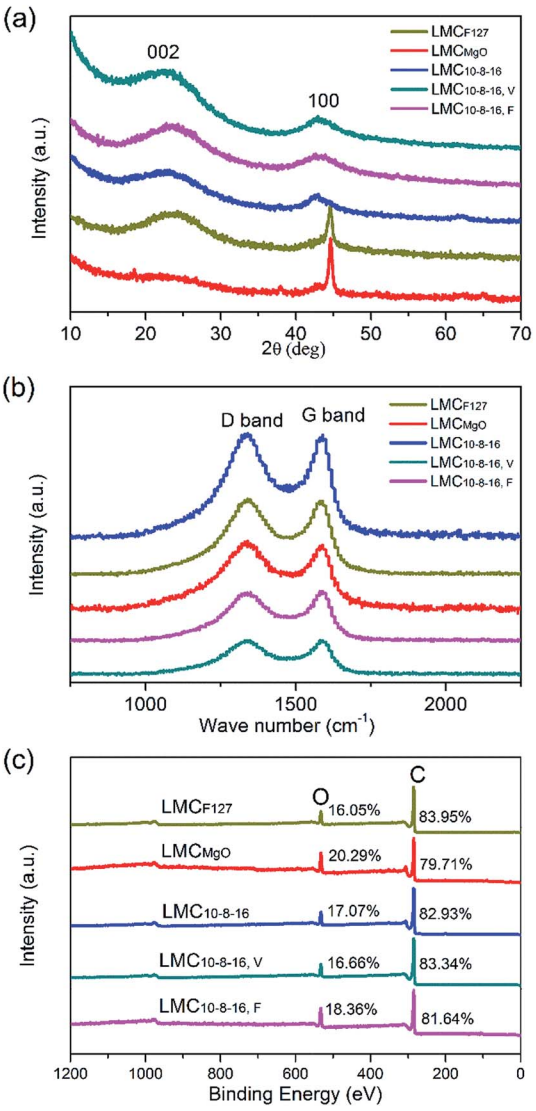

Fig. 5 (a) XRD patterns, (b) Raman spectra, and (c) overall XPS survey spectra for LMCs.

3.2 Electrochemical analysis

We further directly investigated the electrochemical performance in a three-electrode configuration by mixing carbon samples with acetylene black and PTFE together as electrode. Cyclic voltammetry (CV) measurements were carried out at different scan rates ranging from 5 to 100 mV s^{-1} within the potential window of 0 to 0.8 V. At a slow scan rate of 5 mV s^{-1}, samples prepared *via* dual templates route exhibited ultimate capacitance behavior, evidenced by the nearly rectangular shaped plots (Fig. 6a), the typical performance of electric double-layer capacitor[39] (EDLC), suggesting highly reversible charge–discharge responses. When shifting to a faster scan rate of 10 mV s^{-1}, the CV plots shapes of $LMC_{10\text{–}8\text{–}16,\ V}$ and $LMC_{10\text{–}8\text{–}16,\ F}$ tended to deviate from rectangular and gradually form shuttle-shaped plots, especially at the scan rate of 20 mV s^{-1} (Fig. 6b). The CV curve for $LMC_{10\text{–}8\text{–}16}$ still kept more rectangular shape before the scan rate increased to over 50 mV s^{-1}, when it became shuttle shape (Fig. S5a†). The CV plots of selected carbons are shown in Fig. S5b–f.† LMC_{F127}, LMC_{MgO} and $LMC_{10\text{–}8\text{–}16,\ F}$ showed poor charge–discharge responses, evidenced by the triangle-shaped CV plots of LMC_{F127} at any scan rate ranging from 5 to 100 mV s^{-1} and by the shuttle-shaped CV plots of LMC_{MgO} and $LMC_{10\text{–}8\text{–}16,\ F}$ at the faster scan rate. Besides, redox pseudocapacitance peaks were also observed clearly in the CV curves of LMC_{F127}, which can be mainly related to surface oxygen-containing functionalities. LMC_{F127} is consisted of 83.95% C and 16.05% O on the surface. Such a high O content mainly induced the pseudocapacitance behavior of LMC_{F127}. A gradual depression of the plateau values in the CV profiles of all carbons was observed with the increase of scan rate, caused by that the voltage signal couldn't reach the pores effectively and by the ohmic resistance difference between mesopores at the top and at the bottom of the electrolyte under increased scan rate.[36] Fig. 6c shows the relationship between specific galvanostatic capacitance (C_g) and scan rate. Among the five selected typical samples, LMC_{MgO} exhibited the smallest C_g value throughout all scan rates, decreasing from 105.6 F g^{-1} at 5 mV s^{-1} scan rate to 37.3 F g^{-1} at 100 mV s^{-1} scan rate. Though $LMC_{10\text{–}8\text{–}16,\ F}$

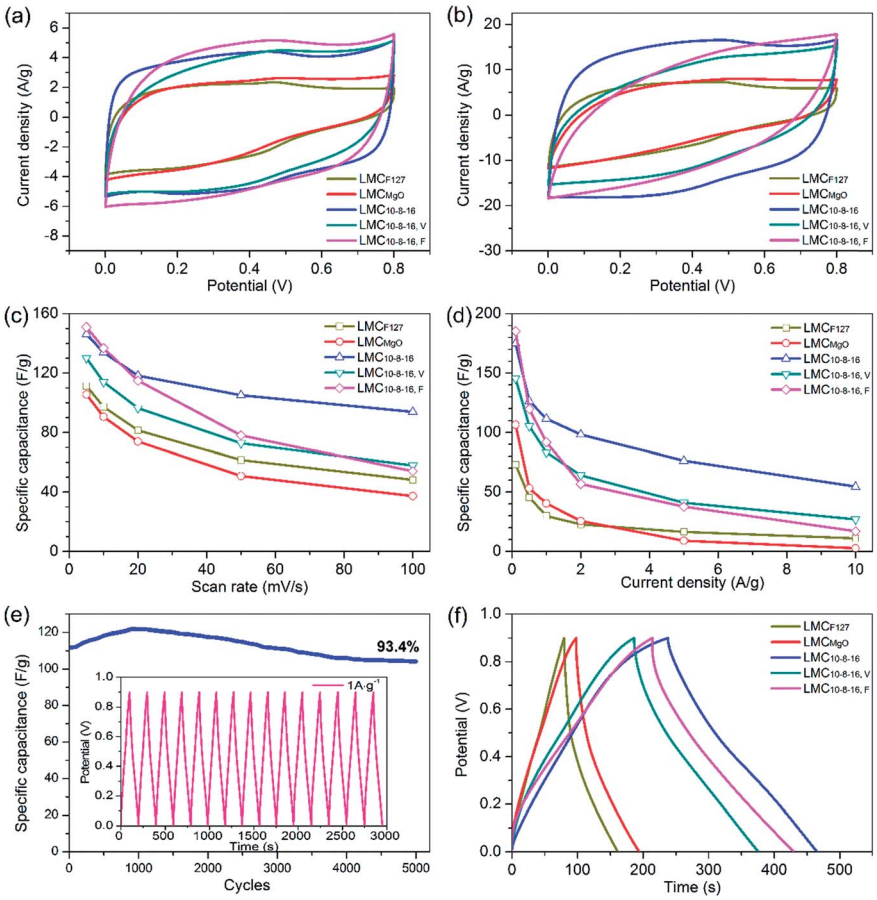

Fig. 6 Cyclic voltammograms of carbons determined in a three-electrode configuration: (a) at 5 mV s^{-1} scan rate, and (b) at 20 mV s^{-1} scan rate; (c) specific capacitance *vs.* scan rate, and (d) specific capacitance *vs.* discharge current density; (e) cyclic performance of $LMC_{10-8-16}$ at a current density of 1 A g^{-1} with the galvanostatic charge/discharge curve shown in inset; (f) galvanostatic charge/discharge curves for carbons at a current density of 0.5 A g^{-1}.

exhibited the largest specific capacitance of 151 F g^{-1} at 5 mV s^{-1} scan rate, the C_g value appeared an apparent sharp decline, and only maintained 54 F g^{-1} at 100 mV s^{-1} scan rate, which rarely reached 57.5% C_g value of $LMC_{10-8-16}$. Saha *et al.*[21] prepared activated mesoporous carbons from pre-cross-linked lignin *via* F127 templating route and further coupled with activation by KOH and CO_2. Though the porosity of these carbons were largely enhanced after activation, the specific capacitance of their optimal carbon was only 100 F g^{-1} at 5 mV s^{-1}, which was still smaller than LMC_{MgO}, the sample with the smallest C_g value among our all samples.

Fig. 6d shows the relationship between specific galvanostatic capacitance and increasing current density and depicts that the C_g value of LMC_{F127} and LMC_{MgO} are still relatively small. At a current density of 0.5 A g^{-1}, $LMC_{10-8-16}$ showed a specific capacitance of 126.4 F g^{-1}, about two times larger than that of LMC_{F127} and LMC_{MgO}. Such poor electrochemical behavior for LMC_{F127} and LMC_{MgO} can be undoubtedly attributed to the small surface area and the lack of capacity for charge storage. Besides, as shown in Fig. 6e, after 5000 cycles at 1 A g^{-1}, $LMC_{10-8-16}$ displayed good electrochemical stability for maintaining 93.4% capacitance retention from the initial C_g value of 111.6 F g^{-1}. The C_g value of $LMC_{10-8-16,\ F}$ still exhibited a sharp decline trend and decreased from 186.3 F g^{-1} at a lower current density of 0.1 A g^{-1} to mere 17 F g^{-1} at the high current density of 10 A g^{-1}. Fig. 6f is the typical triangle-like charge/discharge profiles of obtained carbons at the current density of 0.5 A g^{-1}. Obviously, $LMC_{10-8-16}$ exhibited a longer charge/discharge time for a complete cycle and a better reversible capacitive behavior than the other four samples. Galvanostatic charge/discharge curves at various of current densities of $LMC_{10-8-16}$ were also provided in Fig. S6.† Although sample $LMC_{10-8-16,\ V}$ possesses the largest BET SSA, mesopore and total pore volume, it didn't exhibit a better electrochemical performance than $LMC_{10-8-16}$ through our study. Generally, for an example of the electrochemical behavior of $LMC_{10-8-16}$ and LMC_{F127}, a large specific surface area has a positive impact for storing more charge and therefore performs a better electrochemical behavior. However, not all surface could establish electric double layer. Pore structure connectivity and surface functionalities also have effect on eventual electrochemical performance. As mentioned above, MgO nanoparticles just function as substrates by space occupying effect, and the vacuum environment during solvent evaporation can enhance the uniformity of templates. Pores in $LMC_{10-8-16,\ V}$ are much

regular and isolated, and $LMC_{10-8-16,\ V}$ may have a much poorer pore structure connectivity than $LMC_{10-8-16}$. It is relatively more difficult for $LMC_{10-8-16,\ V}$ to meet the rapid ions transportation, leading to a higher ion-transport resistance and more insufficient ionic diffusion. Furthermore, XPS data indicates the small differences of surface oxygen content in all as-made carbons. Therefore, the better pore connectivity may be the major factor that induced the better electrochemical performance of $LMC_{10-8-16}$ than that of $LMC_{10-8-16,\ V}$.

4. Conclusions

Lignin-derived mesoporous carbons with dominating pore width of 9 nm have been successfully synthesized, the BET SSA and total pore volume of which reached 712 $m^2\ g^{-1}$ and 0.90 $cm^3\ g^{-1}$, respectively. F127 functions mainly to disperse MgO sufficiently and the amount of MgO nanoparticles determines the porosity, which was significantly enlarged in comparison with carbons *via* single template route. The mixing mass ratio of lignin to nano-sized MgO as well as the dosage of F127 plays a major role to enrich the porosity of carbons. Vacuum environment during solvent evaporation enhanced porosity and pore uniformity, but didn't enhance the electrochemical performance. The carbon with atmospheric pressure environment, on contrast, exhibited a better electrochemical behavior. While vacuum freeze drying preserved the skeleton of the entire precursors composite and also significantly hindered the agglomeration of template. The corresponding carbon exhibited a much smaller mesopore and total pore volume but a larger specific capacitance of 186.3 F g^{-1} than those of carbon with atmospheric pressure environment.

Conflicts of interest

There are no conflicts to declare.

Acknowledgements

This work was financially sponsored by the National Science & Technology Pillar Program during the Twelfth Five-year Plan Period (Grant No. 2015BAD14B06).

References

1 S. Solomon, G. K. Plattner, R. Knutti and P. Friedlingstein, Irreversible climate change due to carbon dioxide emissions, *Proc. Natl. Acad. Sci. U. S. A.*, 2009, **106**(106), 1704–1709.

2 R. J. White, V. Budarin, R. Luque, J. H. Clark and D. J. Macquarrie, Tuneable porous carbonaceous materials from renewable resources, *Chem. Soc. Rev.*, 2009, **38**(12), 3401–3418.

3 J. Lorenz, K. Panagiotou and A. Steger, Catalytic Carbonization of Lignin for Production of Electrically Conductive Charcoal, *J. Biobased Mater. Bioenergy*, 2012, **6**(1), 69–74.

4 W. Boerjan, J. Ralph and M. Baucher, Lignin biosynthesis, *Annu. Rev. Plant Biol.*, 2003, **54**(1), 519–546.

5 M. M. Titirici, R. J. White, N. Brun, V. L. Budarin, D. S. Su, F. D. Monte, *et al.*, Sustainable carbon materials, *Chem. Soc. Rev.*, 2015, **44**(1), 250–290.

6 C. O. Tuck, E. Pérez, I. T. Horváth, R. A. Sheldon and M. Poliakoff, Valorization of biomass: deriving more value from waste, *Science*, 2012, **337**(6095), 695–699.

7 J. D. Nguyen, B. S. Matsuura and C. R. J. Stephenson, ChemInform Abstract: A Photochemical Strategy for Lignin Degradation at Room Temperature, *J. Am. Chem. Soc.*, 2014, **136**(4), 1218–1221.

8 H. N. Lyckeskog, C. Mattsson, L. E. Amand, L. Olausson, S. I. Andersson, L. Vamling, *et al.*, The storage stability of bio-oils derived from the catalytic conversion of softwood Kraft lignin in subcritical water, *Energy Fuels*, 2016, **30**(4), 3097–3106.

9 A. Rahimi, A. Ulbrich, J. J. Coon and S. S. Stahl, Formic-acid-induced depolymerization of oxidized lignin to aromatics, *Nature*, 2014, **515**(7526), 249–252.

10 W. Sangchoom and R. Mokaya, Valorization of Lignin Waste: Carbons from Hydrothermal Carbonization of Renewable Lignin as Superior Sorbents for CO_2 and Hydrogen Storage, *ACS Sustainable Chem. Eng.*, 2015, **3**(7), 1658–1667.

11 D. Montané, V. Torné-Fernández and V. Fierro, Activated carbons from lignin: kinetic modeling of the pyrolysis of Kraft lignin activated with phosphoric acid, *Chem. Eng. J.*, 2005, **106**(1), 1–12.

12 D. W. Wang, F. Li, M. Liu, G. Q. Lu and H. M. Cheng, 3D aperiodic hierarchical porous graphitic carbon material for high-rate electrochemical capacitive energy storage, *Angew. Chem., Int. Ed.*, 2008, **47**(2), 373–376.

13 W. Zhang, Z. H. Huang, Z. Guo, C. Li and F. Kang, Porous carbons prepared from deoiled asphalt and their electrochemical properties for supercapacitors, *Mater. Lett.*, 2010, **64**(17), 1868–1870.

14 C. Zheng, Q. Li, M. Yoshio and H. Wang, Cooperation of micro- and meso-porous carbon electrode materials in electric double-layer capacitors, *J. Power Sources*, 2010, **195**(13), 4406–4409.

15 X. J. He, N. Zhao, J. S. Qiu, N. Xiao, M. X. Yu, C. Yu, *et al.*, Synthesis of hierarchical porous carbons for supercapacitors from coal tar pitch with nano-Fe_2O_3 as template and activation agent coupled with KOH activation, *J. Mater. Chem. A*, 2013, **1**(33), 9440–9448.

16 M. J. Valero-Romero, E. M. Márquez-Franco, J. Bedia, J. Rodriguez-Mirasol and T. Cordero, Hierarchical porous carbons by liquid phase impregnation of zeolite templates with lignin solution, *Microporous Mesoporous Mater.*, 2014, **196**(196), 68–78.

17 R. Ruiz-Rosas, M. J. Valero-Romero, D. Salinas-Torres, J. Rodriguez-Mirasol, T. Cordero, E. Morallon, *et al.*, Electrochemical performance of hierarchical porous carbon materials obtained from the infiltration of lignin into zeolite templates, *ChemSusChem*, 2014, **7**(5), 1458–1467.

18 D. Salinas-Torres, R. Ruiz-Rosas, M. J. Valero-Romero, J. Rodriguez-Mirasol, T. Cordero, E. Morallon, *et al.*,

Asymmetric capacitors using lignin-based hierarchical porous carbons, *J. Power Sources*, 2016, **326**, 641–651.

19 H. Li, D. Yuan, C. H. Tang, S. X. Wang, J. T. Sun, Z. B. Li, *et al.*, Lignin-derived interconnected hierarchical porous carbon monolith with large areal/volumetric capacitances for supercapacitor, *Carbon*, 2016, **100**, 151–157.

20 D. Saha, E. A. Payzant, A. S. Kumbhar and A. M. Naskar, Sustainable mesoporous carbons as storage and controlled-delivery media for functional molecules, *ACS Appl. Mater. Interfaces*, 2013, **5**(5), 5868–5874.

21 D. Saha, Y. C. Li, Z. H. Bi, J. H. Chen, J. K. Keum, D. K. Hensley, *et al.*, Studies on Supercapacitor Electrode Material from Activated Lignin-Derived Mesoporous Carbon, *Langmuir*, 2014, **30**(3), 900–910.

22 D. Saha, K. E. Warren and A. K. Naskar, Soft-templated mesoporous carbons as potential materials for oral drug delivery, *Carbon*, 2014, **71**(7), 47–57.

23 W. Libbrecht, A. Verberckmoes, J. W. Thybaut, P. V. D. Voort and J. D. Clercq, Soft templated mesoporous carbons: tuning the porosity for the adsorption of large organic pollutants, *Carbon*, 2017, **116**, 528–546.

24 D. Saha, R. Zacharia and A. K. Naskar, Soft-Templated Mesoporous Carbons: Chemistry and Structural Characteristics, in *Polymer Precursor-Derived Carbon*, American Chemistry Society, Washington, DC, 2014, pp. 61–83.

25 M. Inagaki, M. Kato, T. Morishita, K. Morita and K. Mizuuchi, Direct preparation of mesoporous carbon from a coal tar pitch, *Carbon*, 2007, **45**(5), 1121–1124.

26 T. Morishita, Y. Soneda, T. Tsumura and M. Inagaki, Preparation of porous carbons from thermoplastic precursors and their performance for electric double layer capacitors, *Carbon*, 2006, **44**(12), 2360–2367.

27 W. Zhang, Z. H. Huang, G. Cao, F. Kang and Y. Yang, Coal tar pitch-based porous carbon by one dimensional nano-sized MgO template, *J. Phys. Chem. Solids*, 2012, **73**(12), 1428–1431.

28 He, R. C. Li, J. S. Qiu, K. Xie, P. H. Ling, M. X. Yu, *et al.*, Synthesis of mesoporous carbons for supercapacitors from coal tar pitch by coupling microwave-assisted KOH activation with a MgO template, *Carbon*, 2012, **50**(13), 4911–4921.

29 W. Zhang, Z. H. Huang, G. Cao, F. Kang and Y. Yang, A novel mesoporous carbon with straight tunnel-like pore structure for high rate electrochemical capacitors, *J. Power Sources*, 2012, **204**(204), 230–235.

30 T. Morishita, K. Ishihara, M. Kato and M. Inagaki, Preparation of a carbon with a 2nm pore size and of a carbon with a bi-modal pore size distribution, *Carbon*, 2007, **45**(1), 209–211.

31 B. Wang, J. S. Chen, H. B. Wu, Z. Wang and X. W. Lou, Quasiemulsion-templated formation of α-Fe_2O_3 hollow spheres with enhanced lithium storage properties, *J. Am. Chem. Soc.*, 2011, **133**(43), 17146.

32 Z. Wang, D. Luan, S. Madhavi, Y. Hu and X. W. Lou, Assembling carbon-coated α-Fe_2O_3 hollow nanohorns on the CNT backbone for superior lithium storage capability, *Energy Environ. Sci.*, 2012, **5**(1), 5252–5256.

33 C. R. Zhao, W. K. Wang, Z. B. Yu, A. B. Wang and Y. S. Yang, Nano-$CaCO_3$ as template for preparation of disordered large mesoporous carbon with hierarchical porosities, *J. Mater. Chem.*, 2010, **20**(5), 976–980.

34 G. Yang, H. Han, T. Li and C. Du, Synthesis of nitrogen-doped porous graphitic carbons using nano-$CaCO_3$ as template, graphitization catalyst, and activating agent, *Carbon*, 2012, **50**(10), 3753–3765.

35 S. Tomita, A. Burian, J. C. Dore, D. LeBolloch, M. Fujii and S. Hayashi, Diamond nanoparticles to carbon onions transformation: X-ray diffraction studies, *Carbon*, 2002, **40**(9), 1469–1474.

36 S. Prabaharan, R. Vimala and Z. Zainal, Nanostructured mesoporous carbon as electrodes for supercapacitors, *J. Power Sources*, 2006, **161**(1), 730–736.

37 Y. Fang, Y. Y. Lv, R. C. Che, H. Y. Wu, X. H. Zhang, D. Gu, *et al.*, Two-dimensional mesoporous carbon nanosheets and their derived graphene nanosheets: synthesis and efficient lithium ion storage, *J. Am. Chem. Soc.*, 2013, **135**(4), 1524–1530.

38 G. Eda and M. Chhowalla, Chemically Derived Graphene Oxide: Towards Large-Area Thin-Film Electronics and Optoelectronics, *Adv. Mater.*, 2010, **22**(22), 2392–2415.

39 P. Simon and Y. Gogotsi, Capacitive Energy Storage in Nanostructured Carbon–Electrolyte Systems, *Acc. Chem. Res.*, 2012, **46**(5), 1094–1103.

